OPTICAL AND NEAR-IR IMAGING OF THE DARK GLOBULE CB 52

B. MAIOLO, F. STRAFELLA,[1] L. CAMPEGGIO, AND D. ELIA

Dipartimento di Fisica, Università di Lecce, CP 193, 73100 Lecce, Italy; maiolo@le.infn.it,
strafella@le.infn.it, campeggio@le.infn.it, eliad@le.infn.it

AND

S. AIELLO

Dipartimento di Astronomia e Scienza dello Spazio, Università di Firenze, Italy; Aiello@unifi.it

Received 2006 October 31; accepted 2007 February 7

ABSTRACT

The internal structure of the dark globule CB 52 is investigated by means of broadband imaging in the optical and near-IR spectral range. By exploiting the extinction of the stellar light within this object, we derive observational parameters suitable to infer the internal structure of this cloud. Extinction maps were obtained at different wavelengths by using both stellar counts and two-color diagrams. While in the optical region the extinction is better evaluated at the cloud boundaries, the internal regions are more conveniently probed in the near-IR, so a combined map was derived. The total-to-selective extinction ratio R_V was also observed to increase toward the inner regions, and a plot versus the extinction A_V suggests that grain growth processes are active in this cloud. The statistical fluctuation of the A_V, estimated in the line of sight of the background stars, is investigated by comparing the observed stellar colors with those of the unreddened stars. The dispersion σ_{A_V}, derived from optical observations, is found to be almost independent of the mean extinction, A_V, while by using near-IR data we find a more complex behavior: the σ_{A_V} versus A_V relation increases until $A_V \sim 6$ and then decreases for larger extinctions. This is discussed in the framework of a simple model, suggesting that a clumpy and clustered structure can explain the observations in the inner regions, while outside the cloud the mass distribution remains more homogeneous.

Subject headings: dust, extinction — ISM: clouds — ISM: globules — ISM: individual (CB 52) — ISM: structure

1. INTRODUCTION

Dark clouds are relatively dense interstellar (IS) regions containing molecular gas and dust grains. At optical wavelengths they appear as dark regions projected on rich stellar fields even if, as the wavelength increases, they become more transparent, until the stellar background reappears when observing in the IR spectral region.

Observations of reddened background stars, projected on these clouds, reveal that approximately 1% of their mass is in dust grains, which are often distributed in a hierarchy of substructures, in analogy with the observations of the molecular gas component (see, e.g., Bains et al. 2006). This internal structure (i.e., the way the mass is distributed in these clouds) has been, and still is, the subject of theoretical and observational investigations, even for the close connection between molecular clouds and star formation. It is, in fact, generally recognized that the bulk of the star formation, both in our and in external galaxies, takes place in molecular clouds, so the characteristics of these IS objects become of primary importance for our understanding of the stellar genesis.

The physical parameters usually obtained from the observations of the IS clouds are temperature, density, and chemical composition, as well as their spatial distribution. In addition, the velocities involved in these clouds can be obtained by exploiting the Doppler shift of the emission lines of the gas component.

The values derived for all these quantities characterize these clouds as cold, massive condensations of IS matter, often showing higher density regions, the "clumps," containing in turn even more dense regions, the "cores," with which the star

formation activity seems to be associated. In this scenario, it is not surprising that the same cloud might host multiple formation sites associated with different active cores (see, e.g., Blitz et al. 1984; Testi et al. 2000; Lada & Lada 2003).

The masses and sizes of the molecular clouds span a large range, from giant objects, with masses and radii of the order of $M \sim 10^4$–10^6 $M_\odot$ and $R \sim 100$ pc, to small clouds, with $M \sim 10^0$–10^2 $M_\odot$ and $R \sim 0.1$ pc (see, e.g., Blitz et al. 1984). Typical shapes are irregular for giant clouds and more regular for small clouds, as is the case for the Bok globules with approximately ellipsoidal shapes in a range of sizes $R \sim 0.005$–1 pc.

In the hierachical scenario, in which the clouds are fragmented in clumps and cores, the mass spectrum observed for these substructures is usually approximated by a power law,

$$\frac{dN}{d\ln M} \propto M^{-\alpha}, \qquad (1)$$

where $\alpha = 0.6$–0.8 for clumps and $\alpha = 1.1$ for cores (Williams et al. 2000; Testi & Sargent 1998). Considering that the slope derived for the stellar mass spectrum is $\alpha \sim 1.35$, the intermediate value $\alpha \sim 1.1$, obtained for cores, supports the idea that these objects could represent the final stage of the cloud fragmentation and the first step of the star formation process.

In recent years, particular attention has been paid to the study of the internal structure of the IS clouds in an attempt to better understand the physical mechanisms driving these objects and influencing the star formation. In this sense, structural studies can be of great impact in clarifying important aspects of the star formation process, such as the efficiency, the rate, and the distribution of the stellar masses.

---

[1] Also at IFSI-INAF, Rome, Italy.

In the last decade, several observational studies (Lada et al. 1994; Bazell & Desert 1988; Stutzki et al. 1998; Campeggio et al. 2004) pointed out the possibility of a fractal description of the structure of molecular clouds. According to this approach, the spatial structure of these clouds is autosimilar, and their structural properties remain invariant on the range of spatial scales investigated by the observations.

Some theoretical support for this hypothesis comes from the consideration that, given the values of temperature, density, and velocity involved, the supersonic turbulence should be a common regime in the IS clouds. If this is the case, complex density and velocity fields are expected, with specific statistical properties. These have been recently considered and found to be consistent with the observations (see, e.g., Padoan et al. 1998; Padoan & Nordlund 1999; Heyer & Brunt 2004). In particular, fluido-dynamical models of IS clouds (Padoan et al. 2003), taking into account the turbulence, have been able to explain the complex structures implied by the observed statistical behavior of the extinction A_V (Lada et al. 1994; Campeggio et al. 2004).

In a previous work, we studied the structure of CB 107, a small globule at a distance of $d \sim 180$ pc, projected toward the Galactic center (Strafella et al. 2001; Campeggio et al. 2004). Here we present the results of optical and near-IR observations of CB 52 (Clemens & Barvainis 1988), another dark globule projected toward the outer Galaxy at coordinates $l = 227.8°$ and $b = -8.2°$, whose distance has been estimated to be ~ 1500 pc (Launhardt & Henning 1997). In this way, we contribute to increasing the number of studied objects to ascertain whether the structural parameters obtained from the observations can be used to differentiate the internal structure of the dark clouds.

This paper is organized as follows. In § 2, we describe the observations and give an account of the data analysis procedure, which involves mosaicking and photometry. In § 3, we present the extinction maps obtained for CB 52 using both optical and near-IR observations. In this section we also discuss the statistical behavior of the extinction dispersion and the spatial distribution of the total-to-selective extinction ratio R_V. Section 4 discusses the results in terms of a simple cloud model suitable for simulating the observed relationship between the extinction dispersion σ_{A_V} and the mean extinction $\langle A_V \rangle$. Finally, § 5 summarizes our results.

2. OBSERVATIONS AND ANALYSIS

To investigate the internal structure of the Bok globule CB 52, we obtained a set of images of this cloud at the ESO-NTT telescope (La Silla, Cile) in the B ($\lambda_{\mathrm{eff}} = 4139$ Å), V ($\lambda_{\mathrm{eff}} = 5426$ Å) and I ($\lambda_{\mathrm{eff}} = 7985$ Å) photometric bands by using EMMI (ESO Multi Mode Instrument). A complementary set of near-IR images was also obtained in the J ($\lambda_{\mathrm{eff}} = 12470$ Å), H ($\lambda_{\mathrm{eff}} = 16530$ Å), and K_s ($\lambda_{\mathrm{eff}} = 21620$ Å) bands by using the imaging mode of the SOFI (Son of Isaac) instrument.

The observations were carried out in the nights of 2003 February 6 and 7, with the optical imager equipped with a 4152×4110 pixel CCD and the near-IR camera with a 1024×1024 pixel array. The corresponding scales were $0.1665''$ pixel^{-1} and $0.2920''$ pixel^{-1}, respectively, and the useful field covered by a single frame is $\sim 9' \times 9'$ in the optical region, while in the near-IR it reduces to $4.9' \times 4.9'$. Given the observed angular size and the estimated distance, the physical size of CB 52 is about 3 pc, a value corresponding to a large Bok globule.

For subsequent data analysis and comparison between obscured and transparent lines of sight, the observing strategy was to slightly extend the imaging outside the dark globule, including some of the neighboring stellar field. This required a mapping of the CB 52 region by subsequently pointing the telescope at adjacent positions. In this way, we obtained partially (one-third of a frame) overlapping frames so that the useful region centered on CB 52 was imaged in the six spectral bands by adopting a mosaicking technique.

In particular, in the optical bands two pointings were needed, while five different pointings were necessary in the near-IR due to the smaller field of view covered by SOFI. At each pointing, we adopted a dithering technique, followed by recentering of the dithered frames. The final mosaic was then obtained by registering the overlapping regions to one another by means of affine geometric transformations.

To obtain information on the internal mass distribution in CB 52, we exploited the extinction properties of the dust component, because this is often observed in close association with the gas and is generally considered a good tracer of the total mass distribution in the dark clouds. While this is well established for the general IS medium (Bohlin et al. 1978; Gordon 1995; Kim & Martin 1996), it could be questioned at the smaller spatial scales of the molecular clouds, as is sometime suggested by the observed mismatch between the positions of the gas and dust emission peaks (see, e.g., Beuther et al. 2004; De Buizer 2002). However, here we assume that the dust is a good tracer of the mass distribution inside our cloud, a reasonable assumption at the spatial resolution of our extinction maps.

2.1. Mosaicking and Photometry

To cover a field of view larger than that of the two imagers we used, multiple frames at different pointings were acquired for each photometric band. These were subsequently arranged on a common spatial reference to obtain a final mosaic of the globule with its surroundings. To this end, the dithered frames at each pointing were first recentered and combined to obtain a single composite image. After a similar processing for all the pointings, the resulting images were registered on a common spatial reference, a procedure facilitated by the large spatial overlap adopted between images obtained with adjacent pointings.

Before proceeding with the photometry in the B, V, I, J, H, and K_s spectral bands, the six different mosaics were in turn aligned on a common spatial reference. This is a relatively straightforward procedure when a large set of common and isolated stars is clearly identified in the images to be aligned. In our case, we first registered separately the optical and the near-IR set of images and only subsequently did we establish a common reference frame, by using fiducial stars detected in both the I and J mosaics. The result of this procedure, as applied to the I and J bands, is shown in Figure 1. Note that, due to the different pixel scales of the optical and near-IR instruments, the near-IR images were also rescaled to allow spatial superposition of the detected stars while preserving the flux conservation. At the end of this procedure, we obtained six aligned mosaics (one per filter) useful for deriving positions and fluxes of the detected stars.

The stellar photometry was obtained by using the DAOPHOT package (Stetson 1987), which is particularly suited to take into account both the sky noise and the stellar blending in crowded fields. This is accomplished by fitting to the observed stellar image a modeled point-spread function (PSF) after subtracting the possible contributions inferred by using the PSF fitting of the neighboring stars.

The whole procedure detects and locates brightness variations within an image and thus distinguishes true stellar images from random noise peaks in the data. Bad pixels and nonstellar objects
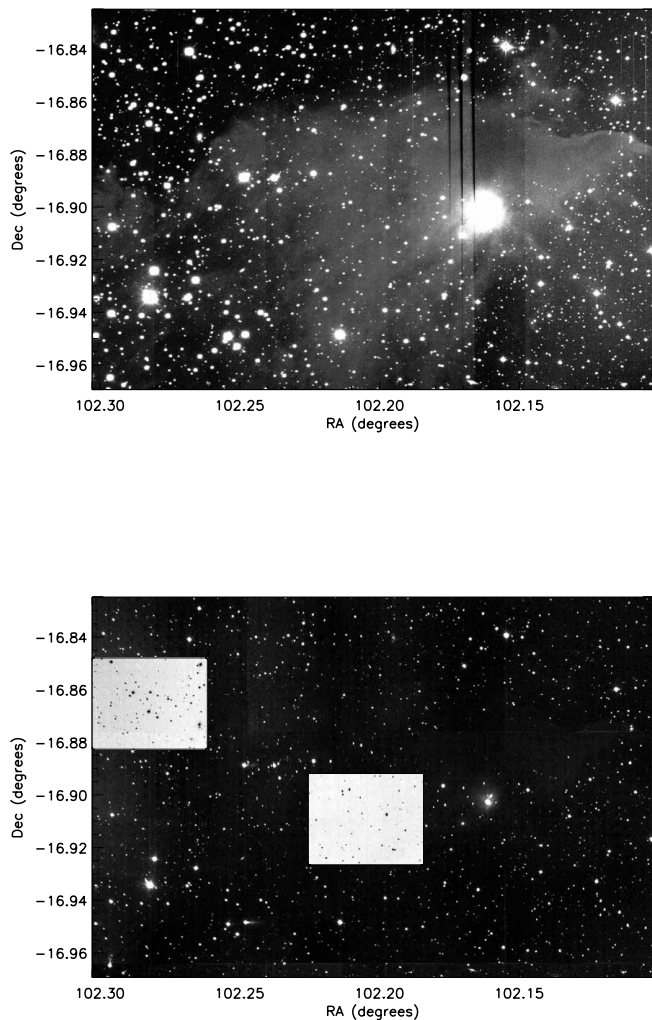
TABLE 1
LIMITING MAGNITUDES

Filter Band	Crowded Region	Dark Region
B	23.5	23.5
V	22.6	23.3
I	21.4	22.4
J	20.4	20.4
H	18.8	18.8
K_s	17.1	17.1

FIG. 1.—Images of the CB 52 field obtained with EMMI and SOFI in the I (*top*) and J bands (*bottom*), respectively. *Bottom*: In negative, two regions. *Top left*: Reference region chosen to evaluate the differential extinctions A_λ by means of stellar counts and to estimate the limiting magnitudes in a crowded region (see Table 1). In the same panel, central part, the region used to estimate the limiting magnitudes in "dark" conditions is shown (see text).

are subsequently rejected on the basis of selection criteria on the shape and sharpness of the detections. In this way we obtained a final list of detected stars, one for each photometric band, with accurate positions and instrumental magnitude values.

To express the brightness in a calibrated magnitude system, during the observing nights we also repeatedly observed standard star fields selected from the Landolt (1992) and Persson et al. (1998) lists, for optical and near-IR observations, respectively. These fields were chosen as near as possible to the position of CB 52 to minimize air-mass differences.

After evaluation of the differential atmospheric extinction coefficients, the photometric zero points zp_λ for the near-IR bands were derived by using the equation

$$m_\lambda = m_i - k_\lambda AM - zp_\lambda, \qquad (2)$$

where m_λ is the magnitude in the standard system, m_i is the instrumental magnitude, k_λ is the extinction coefficient at the given wavelength, λ, and AM is the air mass of the observation.

In addition, in the optical range a color correction was applied to account for the variation in effective wavelength due to

the observation of different spectral shapes. To convert instrumental colors in a standard photometric system, we used the relations

$$V - v = \epsilon(B - V) + zp_v,$$
$$B - V = \mu(b - v) + zp_b,$$
$$V - I = \psi(v - i) + zp_{vi}, \qquad (3)$$

where upper and lower case letters indicate magnitudes in the standard and instrumental system, respectively. The slopes ϵ, μ, and ψ and the zero points zp_v, zp_{bv}, and zp_{vi} were evaluated by observing standard stars with different colors.

2.2. Completeness

By inspecting the optical and near-IR images of CB 52, it is clearly seen that the stellar background is not particularly rich. For our purposes, this is a disadvantage, because our approach exploits the background stars to probe the cloud internal structure through as many lines of sight as possible. This drawback is partially compensated for by the cleaner detection and photometry of the stars, whose brightness distributions are sufficiently separated to avoid the uncertainties due to the confusion affecting more crowded fields.

To correctly determine the extinction by counts, we tested our efficiency in detecting stars as a function of the magnitude. To this end, we investigated the completeness of our detections as a function of the magnitude, by defining as the limiting magnitude the value at which the fraction of detected stars drops to 50% of the total. We also considered two different regions, referred to as "crowded" and "dark," respectively, representative of high and low surface stellar density. These regions, shown in the bottom panel of Figure 1, were used to evaluate possible variations in our ability to detect stars under different background conditions.

In practice, we obtained a completeness function $f(m)$ as the probability for a star, of magnitude m, to be detected in our measurement process (Stetson & Harris 1988; Bolte 1989; Harris 1990). To determine this function, we repeatedly added artificial stars, of known magnitude, to the same images that were subsequently passed to our detection and photometric procedure. The number ratio between the detected and added artificial stars at a given magnitude m_λ is clearly a measure of the corresponding detection completeness. The results obtained for the optical and near-IR bands are shown in Table 1, where "dark" and "crowded" regions are considered separately. Note that in the near-IR bands we find no differences, because the dark region appears transparent at these wavelengths, and its stellar density is comparable to that in the crowded region. On the other hand, in the B band, the stellar surface density is moderate
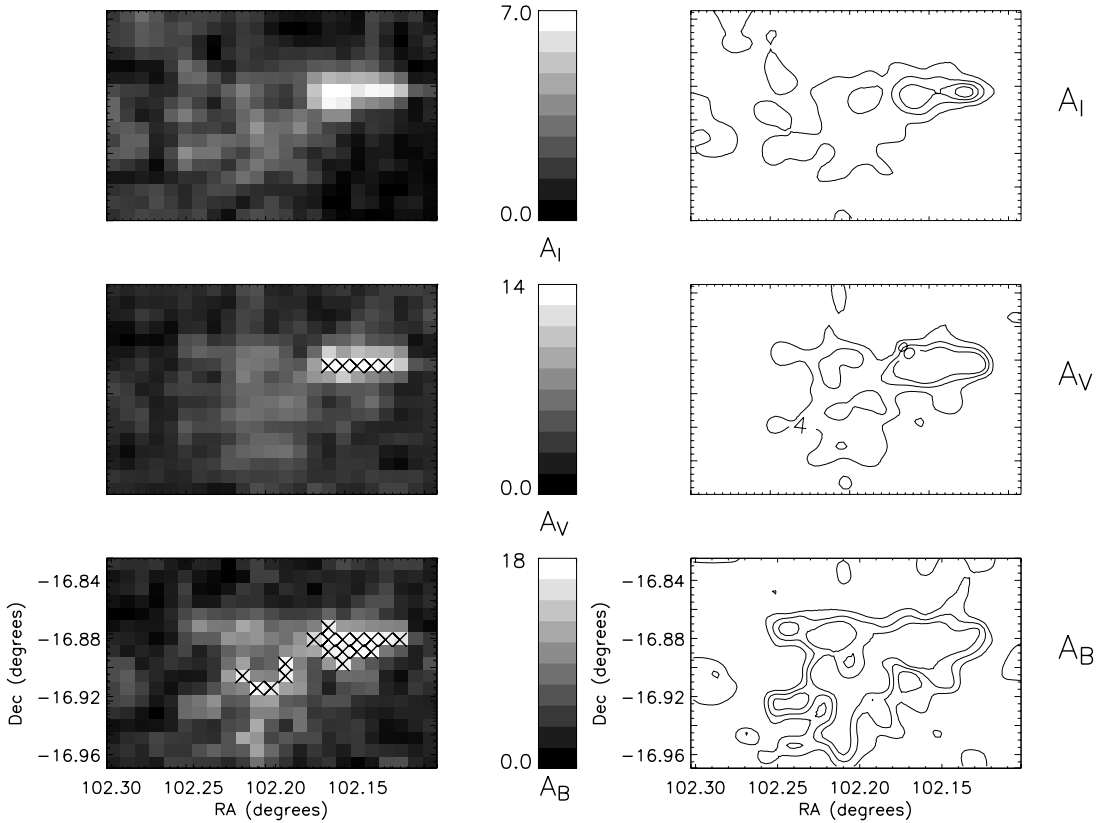
Fig. 2.—Extinction maps obtained by stellar counts in the B, V, and I optical bands (*left, bottom to top*). The corresponding contour maps are shown in the right panels. The lowest contours are drawn for $A_B = 5$ mag, $A_V = 4$ mag, and $A_I = 2.5$ mag, in steps of 2 mag. The box size is $58'' \times 58''$, and a Nyquist sampling (half-size) was used. Boxes marked with a cross are devoid of stars and are left undetermined.

everywhere, and thus the limiting magnitudes are unaffected by crowding.

3. RESULTS

Once the stellar photometry is obtained, the detected stars are counted on a spatial grid and their colors derived by using the spatial correspondence among the aligned images in different filters. Stellar counts and colors are, in fact, the observable quantities we use to infer the spatial distribution of the extinction and to discuss the internal structure in CB 52.

3.1. *The Optical Range*

The extinction map of CB 52 was obtained by using two methods, both based on our ability to evaluate the extinction of the background stars. The first method uses the stellar number density obtained in the boxes of a spatial grid superimposed on the image and thus corresponds to a more or less coarse spatial resolution, depending on the box size. On the other hand, the second method exploits the stellar color excess, which is associated with single lines of sight, and thus carries information on a much smaller spatial scale.

3.1.1. *Extinction Map by Stellar Counts*

This method considers a spatial grid that, superimposed on the image, defines multiple boxes in which the stars are subsequently counted. By comparing the stellar density observed in each box with that obtained in a reference region outside the obscuring globule, it is possible to obtain a differential extinction map of the region, under the assumption of spatial homogeneity for the background stellar population (see, e.g., Lada et al. 1994; Cambrésy 1999; Strafella et al. 2001; Kandori et al. 2003).

In this way, the extinctions, which actually are average values for each grid box, were computed in the optical spectral bands involved in our observations and used to produce the extinction maps shown in Figure 2 for the three optical filters. The box size we used to produce these maps is relatively small ($58'' \times 58''$), paying for the spatial resolution obtained with the loss of the most extinguished boxes in which no stars were counted. This is particularly evident in the B and V maps, in which the crosses mark the undetermined boxes. This drawback can, however, be compensated for by the possibility of using the images at longer wavelengths to determine the extinction in these holes and then producing a combined extinction map.

By dividing the cloud into a total of 23×17 spatial points, the extinction A_λ was determined in each observed band by comparing the stellar surface density d_i in the ith box with the d_{ref} obtained in the reference region. The relationship is

$$A_\lambda(i) = \frac{1}{s_\lambda} \log \frac{d_{\mathrm{ref}}}{d_i}, \qquad (4)$$

where s_λ is the slope of the logarithmic cumulative luminosity function characterizing the stellar background at each wavelength. In practice, the slopes s_λ were evaluated by using the stars detected in the reference region shown as negative in the top left part of the bottom panel in Figure 1. The values we obtained in the optical range are $s_B = 0.190 \pm 0.005$, $s_V = 0.140 \pm 0.002$, and $s_I = 0.173 \pm 0.002$, respectively. By inspecting the extinction maps in Figure 2, we note that the global distribution follows the optical image of the globule, especially in the B and V bands, with some substructures appearing toward the inner higher extinction regions.
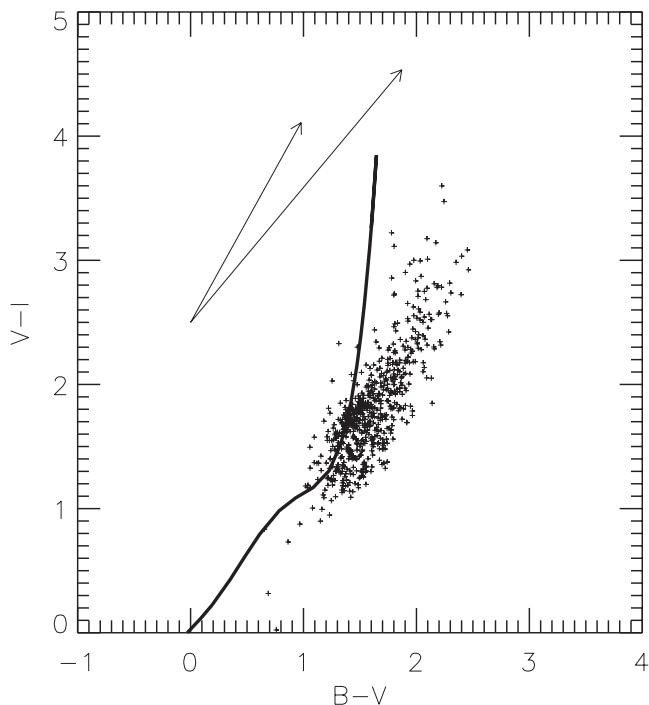
Fig. 3.—$B - V$ vs. $V - I$ two-color diagram for the CB 52 stellar field. The unreddened stellar locus (*solid line*) and the extinction arrows (*top*, $R_V = 6.0$; *bottom*, $R_V = 3.1$) corresponding to $A_V = 5$ are drawn. Only the stars with $B - V > 1.5$ and $V - I > 1.5$ were used to estimate the color excess (see text).

3.1.2. The Color Excess Map

The second method we adopted is based on evaluating the color excess of the background stars, $E_{\lambda_1 - \lambda_2}$, which is a measure of the differential extinction between two wavelengths,

$$E_{\lambda_1 - \lambda_2} = A_{\lambda_1} - A_{\lambda_2}, \qquad (5)$$

where A_{λ_1} and A_{λ_2} are the extinctions at wavelengths λ_1 and λ_2, respectively. Since this quantity is related to the dust column density, it can be used to probe the projected spatial structure of the mass distribution in a dark cloud. In Figure 3 we plot the optical ($B - V$, $V - I$) two-color diagram for stars with $\Delta m < 0.1$ that was used to derive the color excesses.

In this diagram two extinction arrows are also drawn to show the effect of the dust extinction in two possible cases, corresponding to different mean sizes of the dust particles. In the optical range the extinction curve is, in fact, parameterized by the value of R_V, which is observed to vary in the range $2 \lesssim R_V \lesssim 6$ toward lines of sight crossing different environments, the standard value in the diffuse IS medium being $R_V = 3.1$ (see, e.g., Kim & Martin 1996).

The locus of the unreddened stars, as defined by the photometry of Stetson (2000), was also reported to show how the displacements observed with respect to this locus can be used as a measure of the reddening. The lower part of this locus is almost parallel to the reddening vectors and thus cannot be used to determine the stellar color excesses. On the other hand, the upper part is useful, because the reddening lines of the stars with $B - V > 1.5$ and $V - I > 1.5$, crossing the rising part of the locus, can be used more confidently to derive the color excesses.

In doing this, there is actually some ambiguity in cases when the reddening line crosses the unreddened locus twice. In our analysis, however, we considered only the first intersection, cor-
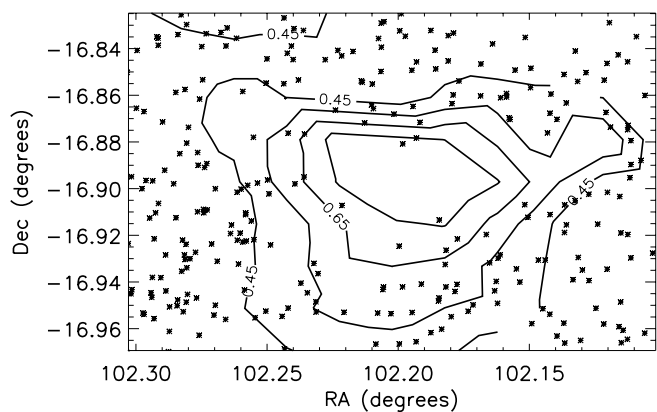

Fig. 4.—Contour levels of $\langle E(B - V) \rangle$ derived as a box average of the stellar excesses obtained by using the color-color diagram in Fig. 3. Due to the lower surface density of the useful stars, the box size used is $110'' \times 110''$. The spatial sampling was obtained by moving the box in steps of half-size (Nyquist sampling), and the starred symbols mark the position of the useful stars. The contours start at $\langle E(B - V) \rangle = 0.45$ and are drawn in steps of $\Delta \langle E(B - V) \rangle = 0.10$.

responding to the rising part of this locus, because in the optical spectral band we statistically probe low extinctions and thus the lower color excesses. Note that, in this case, the component $E(B - V)$ of the reddening vector has practically the same value independently of the particular choice of R_V.

With this method, which corresponds to a high angular resolution, the reddening information is limited to the lines of sight of the useful background stars, and the coverage of the image is irregular and far from complete. Consequently, the field is clearly undersampled, with most of the useful stars located outside the obscured region, as shown in Figure 4, where the iso-$E(B - V)$ contours are also drawn.

3.1.3. The σ_{A_V} versus A_V Relation

Since the two-color diagram allows us to determine a single line-of-sight extinction for a subsample of stars, it is interesting to consider their statistical behavior also, remembering that the spatial scale probed by a single line of sight is very small and that the extinction variations among nearby stars can be used to infer the internal cloud structure. Also in this case we used a partition of the observed field to define spatial boxes in which, considering the color excesses of the stars, we computed the average extinction $\langle A_V \rangle$ and its dispersion σ_{A_V}, assuming the standard value $R_V = 3.1$. The result of this analysis is shown in Figure 5, where the plotted values of σ_{A_V} versus $\langle A_V \rangle$ were obtained with the same box size used to draw the isoexcess contour levels in Figure 4.

This plot shows that the dispersion remains approximately constant regardless of $\langle A_V \rangle$, a statistical behavior typically associated with a smooth spatial distribution of dust (Lada et al. 1994). Different box sizes were also used with similar results. However, note that the useful stars involved in obtaining Figure 5 are preferentially located in regions outside CB 52, in this way probing the environment more than the cloud itself. This is also reflected in the relatively low mean extinction values reported in Figure 5.

3.2. The Near-IR Range

Since the dust grain opacity at 2.2 μm (K_s band) is approximately 1/10 of its value in the V band at 0.5 μm, near-IR observations are clearly more efficient in detecting background stars in the most obscured regions of dark clouds even when, in the optical bands, they appear almost devoid of stars.
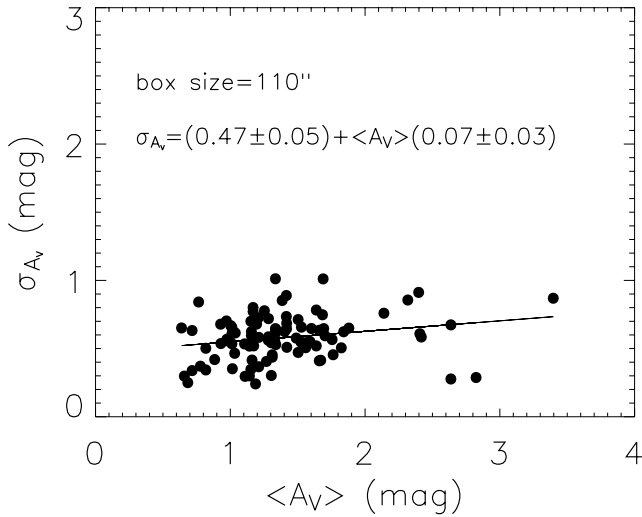
FIG. 5.—Extinction dispersion σ_{A_V} as a function of the mean extinction $\langle A_V \rangle$ derived by means of the color excesses obtained by using the $B - V$ vs. $V - I$ color-color diagram. Only positions with at least three useful stars in the spatial box were considered. This leaves seven positions undetermined.

3.2.1. *Extinction Map by Stellar Counts*

To obtain the CB 52 near-IR extinction maps, we also counted stars, subsequently making use of equation (eq. [4]). In analogy with the optical case, we derived the values of the slope s_λ by fitting, for each wavelength, the magnitude cumulative function of the reference zone. We obtained the values of $s_J = 0.216 \pm 0.003$, $s_H = 0.222 \pm 0.004$, and $s_{K_s} = 0.398 \pm 0.005$ for the three near-IR bands. After taking the same box size adopted for optical images, we corrected the stellar counts for the complete-

ness functions up to the limiting magnitudes in the J, H, and K_s filters (see Table 1). The resulting extinction maps and corresponding contour levels are shown in Figure 6.

Note that, due to the different stellar densities involved in observing at different wavelengths, the extinction values in the inner cloud regions are better determined in the near-IR than in the optical range. This can be exploited to obtain a composite map in which the extinction is reliably determined in both inner and outer regions of the cloud. To this end, we convert the values A_λ, obtained in each box, to the corresponding visual extinctions A_V once the extinction law is given. The extinction values were then used to obtain a weighted map $\langle A_V \rangle$, as we see in § 3.3.

3.2.2. *The $J - H$ versus $H - K_s$ Diagram*

Once the photometry in the J, H, and K_s bands was obtained, the stellar colors were plotted in a two-color diagram. Similar to the optical range, this diagram was used as a tool to estimate the reddening by comparing the stellar positions with the locus of the unreddened stars.

In Figure 7 the $J - H$ versus $H - K_s$ colors for the subset of stars detected in all the near-IR bands, with a photometric uncertainty $\Delta m < 0.1$ mag, are plotted. In further discussions, we consider only the objects located between the two parallel reddening lines delimiting the region in which the unreddened objects are moved by the differential extinction.

In analogy with the optical diagram, in Figure 7 the color excesses are given by the components of the line segment, drawn parallel to the reddening vector, connecting the stellar position with the unreddened locus. One source of uncertainty in this procedure is the shape of the unreddened locus, which in some cases gives rise to two possible intersections with the reddening line. This ambiguity was discussed and its effects quantified in
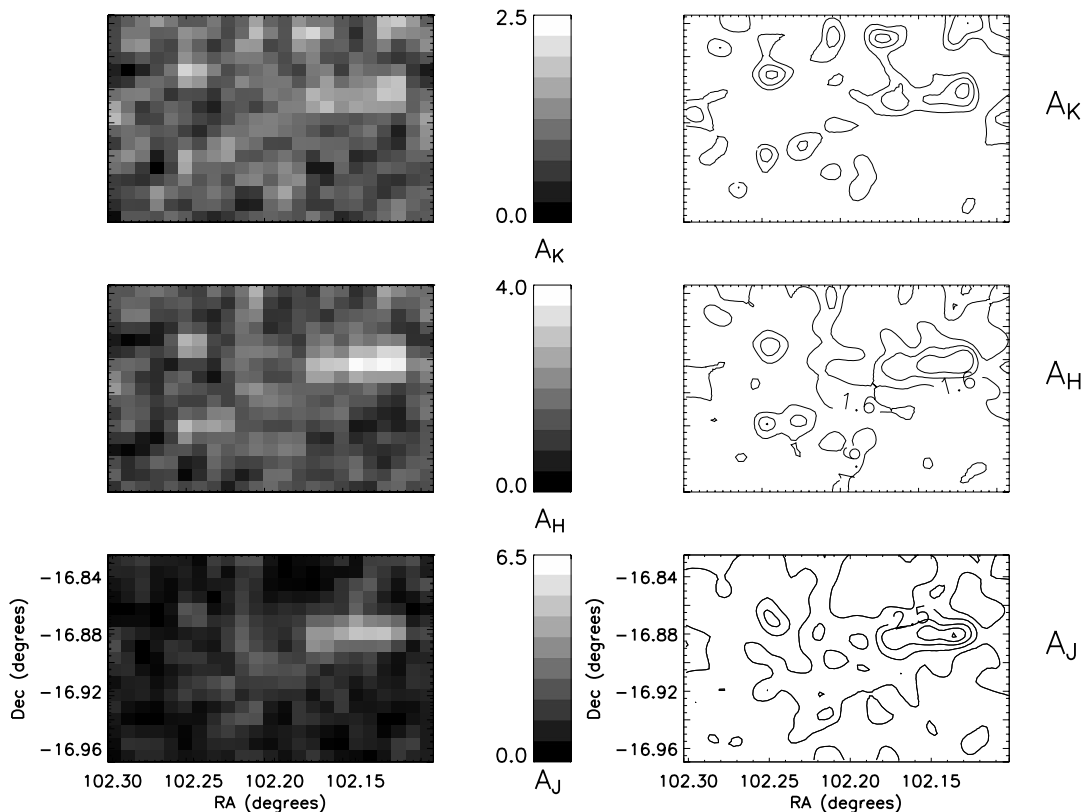
FIG. 6.—Same as in Fig. 2, but for the near-IR bands. The spatial resolution is also the same. The contour levels start at $A_J = 1.5$ mag, $A_H = 1.6$ mag, and $A_K = 1.2$ mag and are drawn in steps of 1.0, 0.8, and 0.4 mag, respectively.
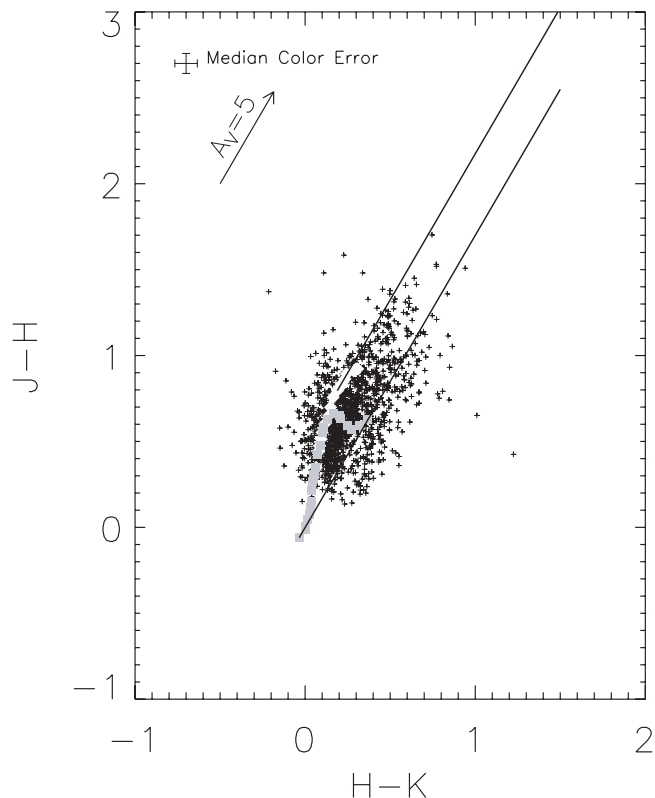
Fig. 9.—CB 52 extinction map obtained by means of the near-IR color excesses derived from the $J - H$ vs. $H - K_s$ diagram. The conversion of the $\langle E_{H-K_s} \rangle$ color excess map of Fig. 8 in this extinction map was obtained by considering the variation of the R_V across the cloud. The box marked with a cross is left undetermined because it contains less than four useful stars. The contours start at $\langle A_V \rangle = 4.5$ mag, with steps of $\Delta \langle A_V \rangle = 1$ mag.

Fig. 7.—$J - H$ vs. $H - K_s$ color-color diagram. The locus of the unreddened stars is plotted with gray symbols. The two lines, drawn parallel to the reddening vector, delimit the region in which the stars are moved by reddening.

Campeggio et al. (2004), who concluded that only a small fraction of objects could be affected by this ambiguity.

Figure 8 illustrates the spatial distribution of the mean color excess $\langle E_{H-K_s} \rangle$ representing the starting point we used to derive another independent version of the extinction map. The conversion of the $\langle E_{H-K_s} \rangle$ color excesses in the corresponding visual extinctions can be obtained simply by means of the relation given by Rieke & Lebofsky (1985),
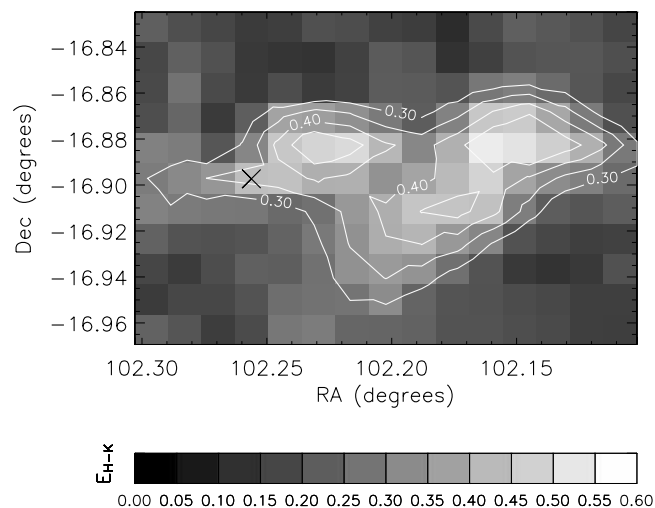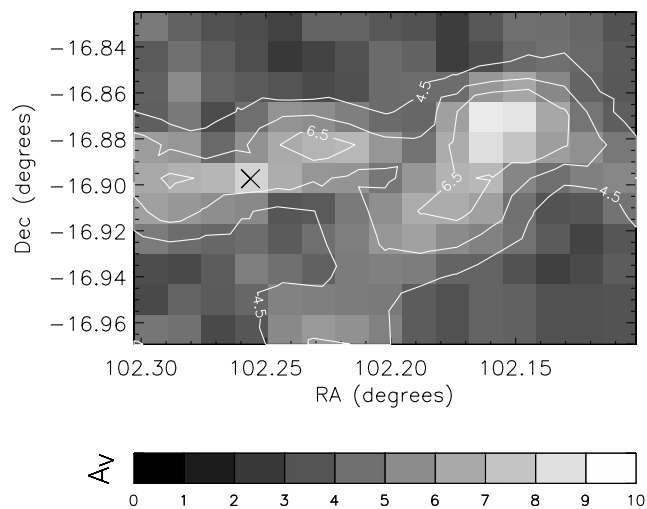
$$A_V = c E_{H-K_s}, \qquad (6)$$

Fig. 8.—E_{H-K_s} map obtained by means of the near-IR two-color diagram in Fig. 7. The box size used is $85'' \times 85''$. The box marked with a cross contains less than four stars and thus is considered undetermined. The contours start at $\langle E_{H-K_s} \rangle = 0.30$ and are drawn in steps of $\Delta \langle E_{H-K_s} \rangle = 0.05$.

with $c = 15.87$, appropriate for a standard reddening curve with $R_V = 3.1$. By scaling the color excesses with this factor, we can easily obtain the corresponding extinction map, which differs from Figure 8 only by this multiplicative constant.

However, because the shape of the extinction curve can differ from the standard case, the constant in equation (6) should be determined accordingly. To take this into account, we computed the appropriate constant in each box of the spatial grid by combining equation (6) with the parameterization of the extinction curve given by Cardelli et al. (1989),

$$\frac{A_\lambda}{A_V} = a_\lambda + \frac{b_\lambda}{R_V}. \qquad (7)$$

Then, for the $H - K_s$ color, we find that the value of the constant for each box of the spatial grid is given by

$$c = \frac{R_V}{R_V(a_H - a_{K_s}) + (b_H - b_{K_s})}. \qquad (8)$$

In this way, the R_V map, which we derive in § 3.4 by using the A_B and A_V maps, allows us to use the H- and K_s-band photometry to derive the extinction map, taking into account the spatial inhomogeneity of the extinction curve across the cloud. In Figure 9 we show the resulting visual extinction map. Both Figures 8 and 9 were obtained by scanning the observed field with a box size $85'' \times 85''$, corresponding to 15×11 positions (Nyquist sampling).

3.2.3. Extinction Dispersion in IR

Since to obtain the extinction map in Figure 9 we used spatial averages of single-star extinctions, we also derived the σ_{A_V}-$\langle A_V \rangle$ relation to consider the fluctuations of the column density across the cloud and then investigate its internal structure. With this aim, we plot the dispersions σ_{A_V} versus the corresponding mean extinctions $\langle A_V \rangle$ computed in each box, evaluating these quantities for both a constant and a variable R_V, as shown in Figure 10 with filled circles and crosses, respectively. The scatter plot obtained
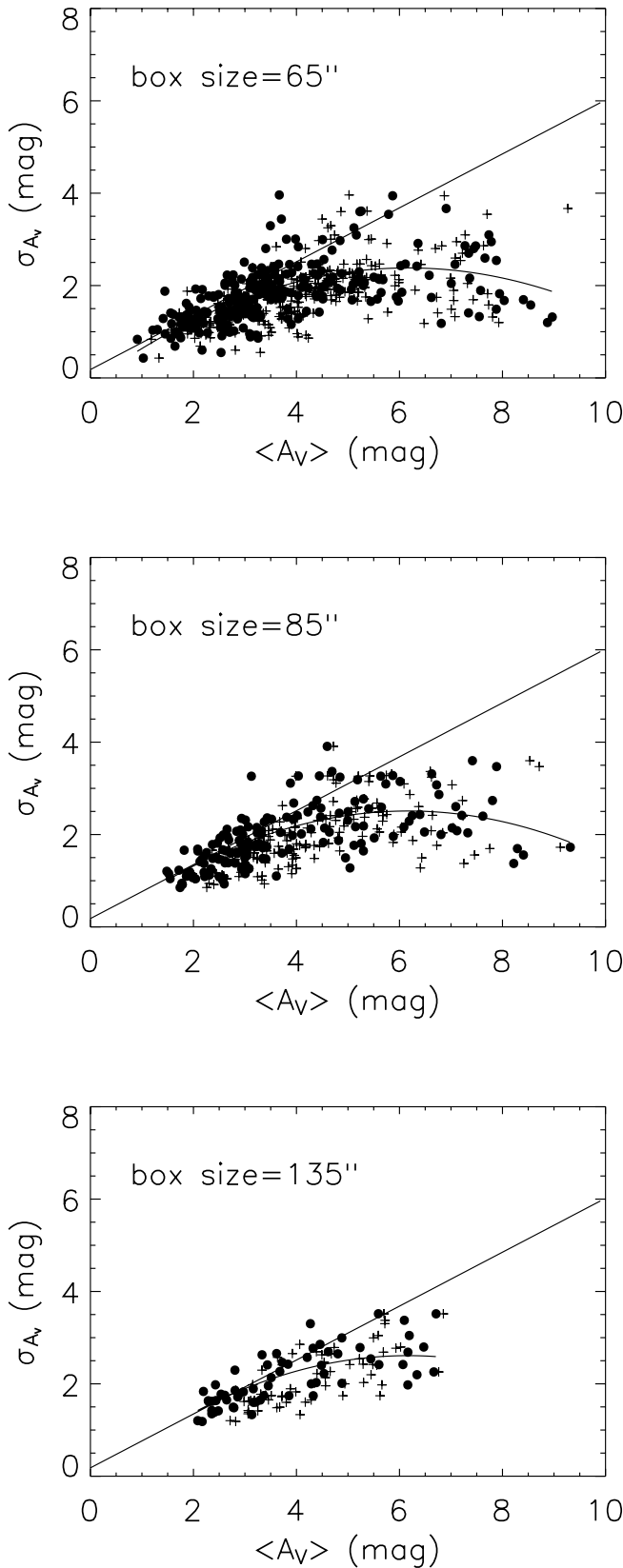
FIG. 11.—Slopes of the σ_{A_V} vs. $\langle A_V \rangle$ relation for different box sizes. The values are the slope of the fitting parabola evaluated at $\langle A_V \rangle = 2$. The triangles are obtained by considering the whole image, while the diamonds represent the values obtained by considering only the cloud in the region with $102.12° < \alpha < 102.22°$ and $-16.94° < \delta < -16.85°$. The error bars are 1 standard deviation and are obtained after 40 iterations with different starting positions of the grid box.

FIG. 10.—Extinction dispersion σ_{A_V} as a function of the mean extinction $\langle A_V \rangle$. The points are obtained by scanning the observed field with the spatial box size reported in each panel, sampling in steps of half this size. The extinctions are derived by the $J - H$ vs. $H - K$ diagram, both assuming a constant $R_V = 3.1$ (circles) and taking into account a variable value for R_V (crosses), as derived by Fig. 13. The continuous line shows the fit of the dark points with a parabola. The straight lines are the tangents at $\langle A_V \rangle = 2$, whose slopes are reported in Fig. 11.
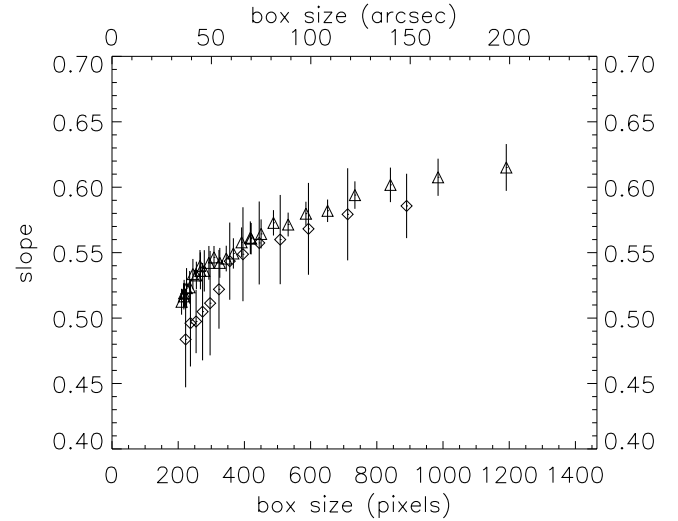
in Figure 10 appears remarkably different from previous plots derived for other clouds (Lada et al. 1994; Alves et al. 1998; Campeggio et al. 2004).

Similar to previous work, we find that the trend for the dispersion is to increase with $\langle A_V \rangle$, the difference being that after a maximum at $\langle A_V \rangle \approx 5.5$–6.5 is reached, the extinction dispersion clearly decreases. Such behavior is observed for the first time here in CB 52, although it has already been envisaged in a model discussed by Lada et al. (1994), who studied the dispersion σ_{A_V} in the neighboring regions of IC 5146. With this model, considering a cloud as composed of a random discrete distribution of dust in high-extinction clumps, Lada et al. (1994) were able to show that, simply by increasing the mean number of clouds intercepted in the lines of sight, the extinction increases, while its dispersion σ_{A_V}, after an increase for low $\langle A_V \rangle$ models, tends to decrease (see their Fig. 10).

To further investigate this case at different spatial scales, we used three different box sizes, 65″, 85″, and 135″, corresponding to the three panels in Figure 10. A characterization of the rising part of these scatter plots was made by approximating the points with a parabola, an arbitrary choice we made only to compare the shape on the different spatial scales. We verified that, by using different box sizes in the range 65″–135″, the vertex of the best-fitting parabola always falls at the same abscissa, within the fitting uncertainties. Because of this, we fixed its value to $\langle A_V \rangle = 6.2$, a choice that allows us to compare, at a given $\langle A_V \rangle$, the slopes of the parabolas obtained for different choices of the box size. The slopes obtained at $\langle A_V \rangle = 2$, as a function of the box size, are plotted in Figure 11, which also shows that the shape of the fitting parabola is practically independent of the box size.

3.3. Combining Optical and Near-IR Information

The information contained in the extinction maps shown in Figures 2 and 6 can be arranged to obtain a combined extinction map. To this end, we averaged, pixel by pixel, the extinction values derived in the different spectral bands, adopting as
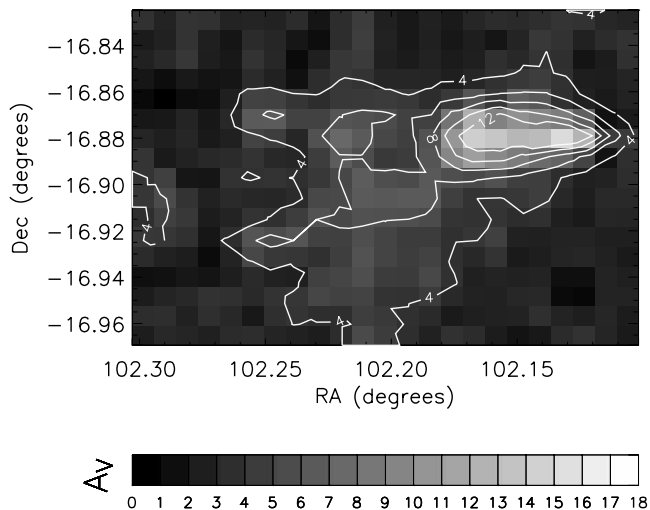
FIG. 12.—Combined extinction map. The extinction in each pixel is obtained as a weighted mean of the six values derived by counting stars in the *B*, *V*, *I*, *J*, *H*, and *K*$_s$ bands. The contours start at $A_V = 4$ and are drawn in steps of $\Delta A_V = 2$.

a weighting factor the fraction of stars counted in each box for each band. Then the averaged extinction in a box was obtained by

$$\langle A_V \rangle_{\text{combined}} = \frac{\sum w_\lambda A_\lambda C_\lambda}{\sum w_\lambda}, \qquad (9)$$

where the weights w_λ in a given grid box are

$$w_\lambda = \left(\frac{n_{\text{box}}}{N}\right)_\lambda C_\lambda \qquad (10)$$

and the index λ runs over the six spectral bands we consider. In the preceding, the variables n_{box} and N are the number of stars in the generic box and the total number of stars in the corresponding spectral band, respectively. The constants $C_\lambda = A_V/A_\lambda$ were obtained by using equation (7) and the R_V values derived from the map in Figure 13.

This procedure offers two advantages. The first is that the constraint on the box size due to the low stellar density in the optical bands is alleviated. The second is that this weighting scheme allows a more reliable determination of the extinction map, because the optical observations are more sensitive to the low column densities typical of the boundaries, while the near-IR observations allow a more accurate mapping of the innermost regions. The composite map we obtained is shown in Figure 12.

The global appearance of the combined map is maintained even if the details can differ with respect to the maps in Figures 2 and 6. In particular, it is noteworthy that all the pixels are now determined in the combined map.

3.4. *Total to Selective Extinction*

The dust extinction properties are parameterized by the ratio of the total to selective extinction,

$$R_V = \frac{A_V}{A_B - A_V} = \frac{A_V}{E_{B-V}}. \qquad (11)$$

It has been shown by Cardelli et al. (1989) that the IS extinction is quite well described by only this parameter, so that it is largely adopted to characterize the observed extinction curves. In our
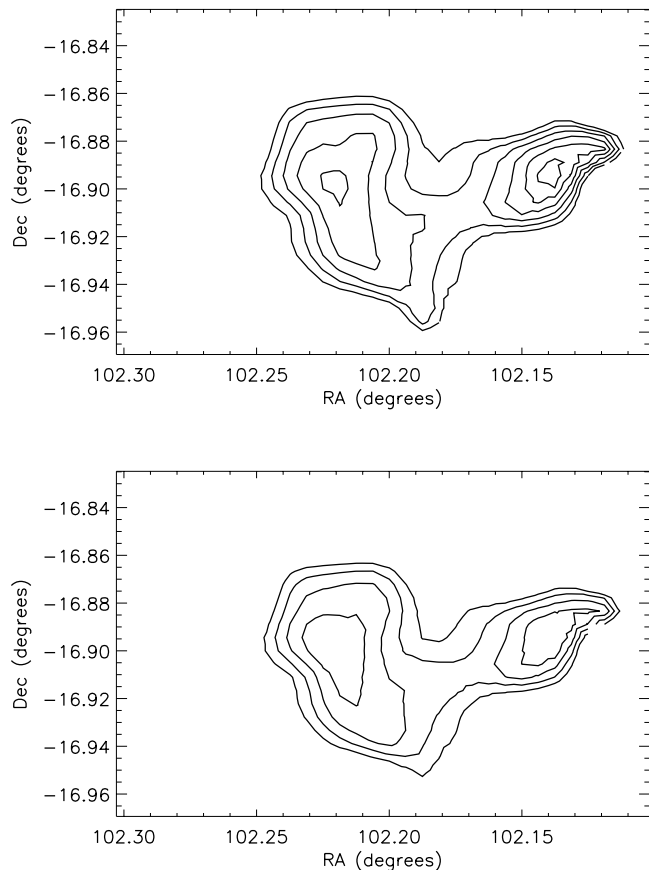

FIG. 13.—Total-to-selective ratio extinction maps. *Top*, R_V derived by using the *B* and *V* extinction maps obtained by stellar counts; *bottom*, same as top, but obtained by using the *B*, *V*, and *K*$_s$ extinction maps (see eq. [12]). The box size used here was chosen ~110″ to avoid the undetermined positions that are seen, with a smaller box size, in Fig. 2. The Nyquist sampling is such that the number of pixels in these maps is 11 × 9. In both panels, the contours start at $R_V = 3$ and are drawn in steps of $\Delta R_V = 0.5$.

case, to determine the spatial behavior of this parameter across CB 52, we could simply use the A_B and A_V maps shown in Figure 2. However, to avoid the undetermined positions seen in the *B* and *V* maps of this figure, we preferred to use a coarser grid, obtaining a map of 11 × 9 pixels (Nyquist sampling).

The resulting R_V map is shown as contour levels in the top panel of Figure 13, where only contours for regions with $A_V > 1.5$ mag and $E(B-V) > 0.1$ mag are drawn. This is because the uncertainties in the value of R_V grow sensitively with decreasing values of the total extinction, as discussed in Larson & Whittet (2005).

Despite these constraints, the large-scale morphology of the globule can be recognized also in this coarse R_V map, with interstellar-like values defining the lowest contour. The fact that R_V increases toward the inner region of the globule can be interpreted as the signature of the presence of larger size grains in the densest regions of the cloud with respect to the external medium (see, e.g., Tielens 1989; Cardelli & Clayton 1991). To check this point, we also used our K_s-band photometry to exploit another remarkable relationship (see Whittet & van Breda 1978) to obtain an alternative estimate of R_V, namely,

$$R_V = 1.1 \frac{E_{V-K_s}}{E_{B-V}}. \qquad (12)$$

The corresponding contour levels we obtained are shown for comparison in the bottom panel of Figure 13. Clearly, both
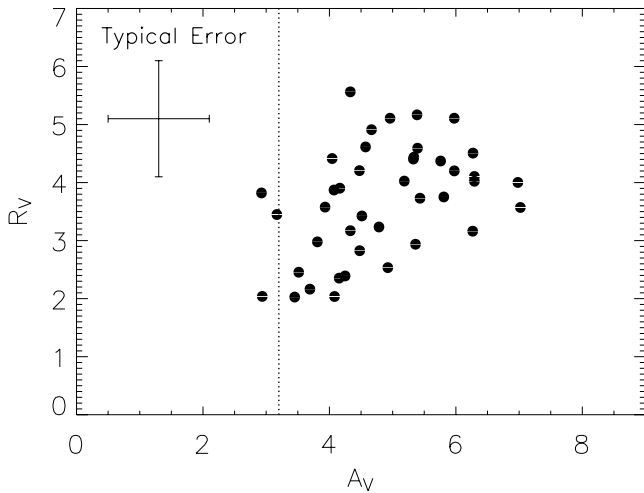
FIG. 14.—R_V vs. A_V relation. The extinction values are obtained as in Fig. 9, but by adopting the coarser grid used to derive the R_V values in Fig. 13. The vertical line represents the threshold extinction for the survival of ice mantles on IS grains.

panels show a similar trend for R_V, with values typically increasing toward the regions with the highest A_V, suggesting that grain growth processes are active in the densest regions of CB 52. The relationship between R_V and A_V has already been studied in the literature to investigate the variations of the extinction curve with the environment (e.g., Vrba et al. 1993; Kandori et al. 2003). In Figure 14 we show the case of CB 52 in which, despite the large typical uncertainties in both axes ($\Delta A_V \sim 0.8$ mag and $\Delta R_V \sim 1$), a correlation between these two quantities is actually present, as already found by Kandori et al. (2003) in the star-forming part of the dark cloud L1251. In this respect, it is interesting to note that some *IRAS* sources are also associated with CB 52, and at least one of these is classified as a Class II young stellar object (YSO; Yun & Clemens 1995). In Figure 14 a vertical line denotes the threshold extinction value discussed by Whittet et al. (2001) for ice mantles to survive on IS dust grains, and the positions of our points beyond the threshold suggests that the increase of R_V with A_V is due to the growth of the grain mantle with the column density.

4. DISCUSSION

The results of our analysis, based on the observation of the stellar background, can be reasonably interpreted in the light of a simple model originally suggested by Lada et al. (1994) to discuss the internal structure of a dark cloud in the neighborhood of IC 5146. These authors analyzed some possible density distributions, including the case of a uniform distribution that was clearly unable to interpret the observed σ_{A_V} versus A_V scatter plot. Even describing the cloud as composed of an increasing number of high-density clumps, they were not able to reproduce the observations. These were instead better explained by assuming that, in each box of their spatial grid, a two-dimensional power-law function of the form $A_V(x,y) \propto x^\alpha y^\alpha$ describes the extinction distribution. Here we revisit the clump model because this offers an immediate and more straightforward physical interpretation.

4.1. *The Model*

We consider a cloud as a collection of small spheres (clumps), each one described by a set of parameters as the spatial position, the central density n_0, and the density profile $n(r)$. In our approach, this profile has been described by $n(r) = n_0/[1 + (r/a)^\alpha]$,

where r, a, and α are the radial distance, the scale radius, and the density law exponent, respectively. In this model a given volume of space is filled with a number of spherical clumps, randomly distributed and characterized by a range of parameter values. The clumps are modeled with central densities n_0 chosen by means of a Monte Carlo technique to follow a power-law distribution $N_{clumps} \propto n_0^{-\gamma}$ centered on the mean value $n_c = \langle n_0 \rangle$. The scale radius a can also be varied around its central value a_c, according to the relationship $a = a_c(n_c/n_0)$, an arbitrary choice that, however, allows us to limit somewhat the size of the clumps with the largest central densities.

The other model parameters α and a_c can also be varied, although here we only explore a limited range of reasonable values for a_c and assume that the clumps are spatially limited by their scale radius. With this assumption, we limit somewhat the exploration of the parameter space in the perspective to ascertain, at least qualitatively, whether the observed σ_{A_V} vs. A_V relation is consistent with a clumpy cloud model.

To this end, a code has been developed that determines the column densities involved in a given direction once the three-dimensional clump mass distribution has been generated and projected on the sky plane. Once the line of sight is defined, the intercepted clumps are determined and their impact parameters used to compute the individual contributions to the column density. These are subsequently accumulated to obtain the total value in a given direction so that, by repeating this procedure for different lines of sight, we obtain a simulated column density map. Our simulation is completed by considering an artificial stellar background characterized by density, magnitudes, and colors similar to those actually observed for the stars in the control field outside the dark region of CB 52. This artificial background is randomly distributed on the simulated image, defining in this way the lines of sight for computing the extinction of the stellar light in crossing the intercepted clumps. These simulations have shown that different behaviors can be obtained in the σ_{A_V} versus $\langle A_V \rangle$ relation with appropriate choices of the model parameters.

In Figure 15 we show some examples of simulated images of clouds composed of 4000 clumps, with mean central densities in the range $n_c = 10^3$–10^7 cm^{-3}. In the top three panels, which correspond to a random spatial distribution of the clumps, the decrease of the average clump size a_c, together with an increase in the central densities n_c, produces an increase of the slope in the σ_{A_V} versus $\langle A_V \rangle$ scatter plot. On the other hand, the effects of a specific mass distribution obtained by increasing the clump number density toward the cloud center are shown in the last panel. This kind of behavior is reminiscent of that observed in CB 52, suggesting that a clumpy cloud is a viable possibility.

However, we remark that such behavior is not necessarily an indication of a clumpy structure, because it is actually related to the spatial column density distribution which, in principle, could be due to other different internal structures. In fact, what seems to be important in this context is the presence of a large-scale gradient in column density, followed by a flattening toward the cloud center. These conditions produce low- and high-extinction regions in the same image, the latter being located in the central part of the cloud and being responsible for both large A_V and low σ_{A_V} values.

4.2. *Implications for the Internal Structure*

In comparing our results with previous studies, we first refer to Lada et al. (1999), who derived the σ_{A_V} versus $\langle A_V \rangle$ relationship in IC 5146. They revisited this object, investigating different spatial scales and obtaining a decrease in the slope values from
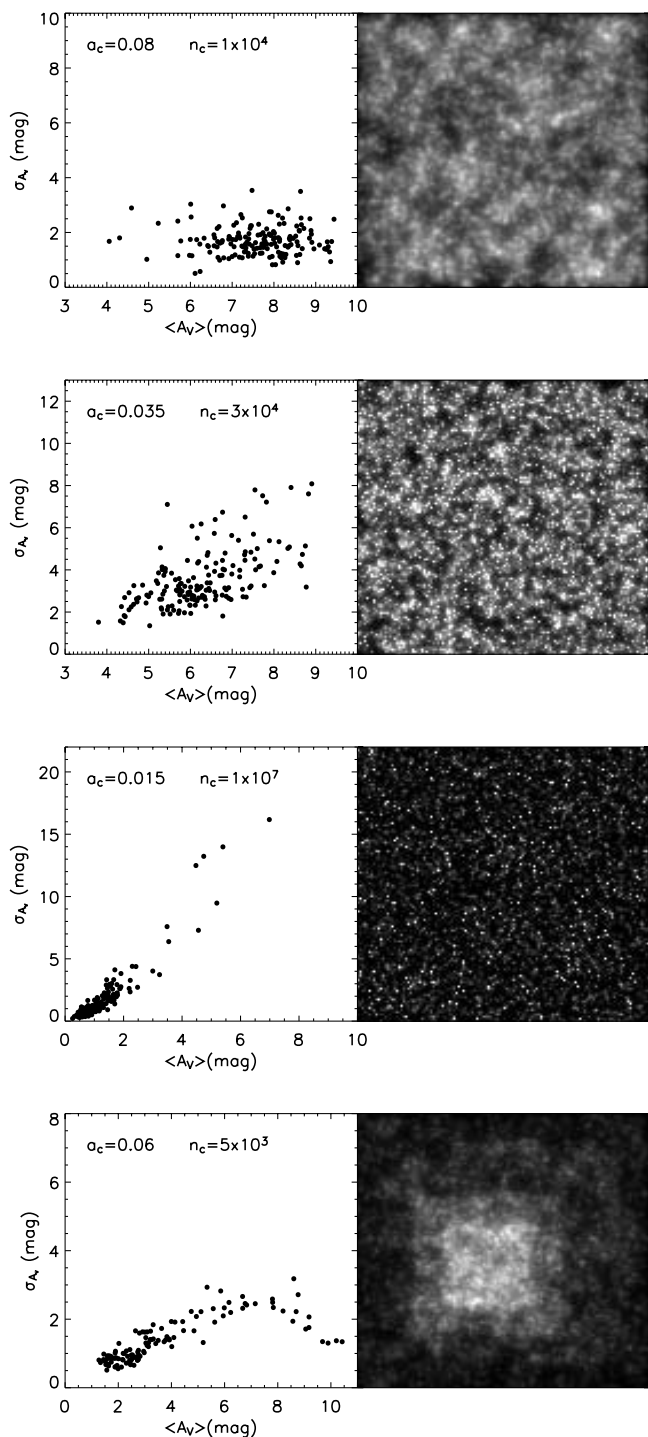
FIG. 15.—Simulated clouds. The relationship between the extinction dispersion σ_{A_V} and the mean extinction $\langle A_V \rangle$ is shown in the left panels for four different model clouds whose appearance, in terms of column density maps, is shown in the right panels. The spatial distribution of the clump centers is random and is the same for the three uppermost panels. The bottom panel is an example of a clustered distribution obtained by simply adding more clumps toward the center. The mean radius a_c and central density n_c of the clumps are reported in each case.

along the same line, Campeggio et al. (2004) studied the slope variation with the spatial resolution in CB 107, obtaining evidence for a decreasing value with increasing spatial resolution.

The slope-size relation, obtained here for CB 52, is shown in Figure 11. This is based on the slope of the fitting parabola, and then its absolute value cannot be directly compared with the values obtained from previous studies by linear fitting. However, it is noteworthy that also in CB 52 we find a trend for the slope to decrease with decreasing box size, noting that this behavior appears relatively smoother than in the other studied cases. Because the estimated distance of this globule is $d \sim 1500$ pc (Launhardt & Henning 1997), the spatial scales investigated correspond to larger physical sizes, suggesting that either the structure of this cloud differs from the other studied cases or the interstellar clouds behave differently at the different spatial scales probed. To quantify, adopting the distance estimates in Campeggio et al. (2004, their Table 2), we find that the scale ranges investigated are 0.09–0.17 pc, 0.22 pc, 0.03–0.17 pc, and 0.3–1.4 pc for IC 5146, L977, CB 107, and CB 52, respectively.

In our modeling we find that, when the clumps are distributed randomly in space we can obtain approximately linear scatter plots, while when the clumps are clustered as in the bottom panel of Figure 15, we observe a curvature of the σ_{A_V} versus $\langle A_V \rangle$ relation. This last case, which we actually observe in CB 52, can then be understood as a variation of the clump projected density within the same cloud, a case that in Figure 15 is obtained simply by concentrating the clumps toward the center.

Note that, because our model is not self-consistent in the fluidodynamical sense, the clumps have been arbitrarily added in the cloud center. Despite this, we think it is acceptable, because the increase of the column density toward the center is observational evidence in Bok globules.

In analogy with the observations, the simulated cloud images have been analyzed with the same procedures to obtain the spatial variation of the extinction, as well as its dispersion in each box. A scatter plot of these two quantities is also shown in Figure 15, which illustrates the trend implied by different choices of the parameter values. As expected, when the cloud appears smooth as in the top panel, the extinction dispersion is almost independent of the mean extinction, while as the homogeneity decreases, we observe a clear modification of the σ_{A_V} versus $\langle A_V \rangle$ relation. This is visualized in the subsequent panels showing, from top to bottom, that the trend in the scatter plot changes progressively until it becomes almost linear in the last panel. It is remarkable that the shapes of the different scatter plots in Figure 15 are reminiscent of the different kinds of observed σ_{A_V} versus $\langle A_V \rangle$ relationships reported in the literature (Lada et al. 1994; Alves et al. 1998; Campeggio et al. 2004). In particular, the bottom panel shows a trend similar to that shown in Figure 10.

Of course, the present modeling is quite heuristic and only shows that a clumpy cloud can explain the observations reasonably. We think that definite conclusions can be only given by more consistent fluidodynamical models that produce the clump distribution we now assume.

Note that in CB 52 we actually find two different trends in the scatter plots in Figures 5 and 10, depending on the spectral region we use to evaluate the extinctions of the background stars. This apparent discrepancy can be reconciled when we consider that the spatial distribution of the background stars we use is different in the optical and near-IR spectral regions (see § 3.1.3) in that the optical stars are mainly detected outside the obscuring cloud. Because of this, the lines of sight probed by the optical stars have little to do with the internal structure, while the

0.41 to 0.18, with box sizes decreasing from $90''$ to $30''$, respectively. This result has been interpreted on the basis of a cylindrical model cloud, implying a smooth large-scale column density gradient, in this way showing that it is not necessary to invoke a small-scale structure.

In another cloud, L977, investigated with a box size of $90''$, Alves et al. (1998) determined a similar value for the slope and,

near-IR stars, being more uniformly detected in the investigated field, are more suited to probe the innermost structured regions.

Finally, we remark that the value of the parameter R_V, which characterizes the steepness of the extinction curve between the B and V spectral bands, increases with increasing extinction, suggesting that the mean size of the dust grains is larger in the inner and denser regions of this cloud, where the grain growth processes are presumably more active.

5. CONCLUSIONS

In this work, the distribution of dust in the Bok globule CB 52 has been studied by exploiting the extinction of the stellar background. To this end, both counting techniques and optical and near-IR color-color diagrams have been used to investigate the projected cloud structure.

By counting stars, we obtained the extinction maps at different wavelengths ($B, V, I, J, H,$ and K_s) that were used to derive a combined extinction map. The R_V map was also obtained, indicating that the R_V value systematically increases toward the center of CB 52, suggesting a corresponding increase in the average size of the dust grains.

By plotting R_V versus A_V, we find that the relationship is similar to that derived by Kandori et al. (2003) in the star-forming part of L1251, an interesting coincidence if we consider that CB 52 is also associated with YSOs.

The $J - H$ versus $H - K$ diagram has also been exploited to obtain the extinction toward the line of sight of single stars. In this way, it is possible to study the relationship between the mean extinction and its dispersion. We find for the first time in CB 52 a peculiar behavior with respect to that observed in the few other clouds studied in the literature. In fact, after an initial trend of increasing with $\langle A_V \rangle$, the σ_{A_V} decreases at the larger extinctions. This can be understood in the framework of a simple model with a large-scale column density gradient, which flattens at the cloud center.

Finally, the slope of the σ_{A_V} versus $\langle A_V \rangle$ relation was investigated as a function of the box size used. This relation is significantly smoother than in the other clouds studied, even if the differences in the spatial scales investigated, implied by the large distance of CB 52 ($d \sim 1500$ pc), prevent unambiguous conclusions about possible differences in the internal structure.

REFERENCES

Alves, J., Lada, C. J., Lada, E. A., Kenyon, S. J., & Phelps, R. 1998, ApJ, 506, 292
Bains, I., et al. 2006, MNRAS, 367, 1609
Bazell, D., & Desert, F. X. 1988, ApJ, 333, 353
Beuther, H., Schilke, P., & Wyrowski, F. 2004, ApJ, 615, 832
Blitz, L., Magnani, L., & Mundy, L. 1984, ApJ, 282, L9
Bohlin, R. C., Savage, B. D., & Drake, J. F. 1978, ApJ, 224, 132
Bolte, M. 1989, ApJ, 341, 168
Cambrésy, L. 1999, A&A, 345, 965
Campeggio, L., Strafella, F., Elia, D., Maiolo, B., Cecchi-Pestellini, C., Aiello, S., & Pezzuto, S. 2004, ApJ, 616, 319
Cardelli, J. A., & Clayton, G. C. 1991, AJ, 101, 1021
Cardelli, J. A., Clayton, G. C., & Mathis, J. S. 1989, ApJ, 345, 245
Clemens, D. P., & Barvainis, R. 1988, ApJS, 68, 257
De Buizer, J. M. 2002, BAAS, 34, 1320
Gordon, M. A. 1995, A&A, 301, 853
Harris, W. E. 1990, PASP, 102, 949
Heyer, M. H., & Brunt, C. 2004, ApJ, 615, L45
Kandori, R., Dobashi, K., Uehara, H., Sato, F., & Yanagisawa, K. 2003, AJ, 126, 1888
Kim, S. H., & Martin, P. G. 1996, ApJ, 462, 296
Lada, C. J., Alves, J., & Lada, E. A. 1999, ApJ, 512, 250
Lada, C. J., & Lada, E. A. 2003, ARA&A, 41, 57
Lada, C. J., Lada, E. A., Clemens, D. P., & Bally, J. 1994, ApJ, 429, 694
Landolt, A. U. 1992, AJ, 104, 340
Larson, K. A., & Whittet, D. C. B. 2005, ApJ, 623, 897

Launhardt, R., & Henning, T. 1997, A&A, 326, 329
Padoan, P., Boldyrev, S., Langer, W., & Nordlund, A. 2003, ApJ, 583, 308
Padoan, P., Juvela, M., Bally, J., & Nordlund, A. 1998, ApJ, 504, 300
Padoan, P., & Nordlund, A. 1999, ApJ, 526, 279
Persson, S. E., Murphy, D. C., Krzeminski, W., Roth, M., & Rieke, M. J. 1998, AJ, 116, 2475
Rieke, G. H., & Lebofsky, M. J. 1985, ApJ, 288, 618
Stetson, P. B. 1987, PASP, 99, 191
———. 2000, PASP, 112, 925
Stetson, P. B., & Harris, W. E. 1988, AJ, 96, 909
Strafella, F., Campeggio, L., Aiello, S., Cecchi-Pestellini, C., & Pezzuto, S. 2001, ApJ, 558, 717
Stutzki, J., Bensch, F., Heithausen, A., Ossenkopf, V., & Zielinsky, M. 1998, A&A, 336, 697
Testi, L., & Sargent, A. I. 1998, ApJ, 508, L91
Testi, L., Sargent, A. I., Olmi, L., & Onello, J. S. 2000, ApJ, 540, L53
Tielens, A. G. G. M. 1989, in IAU Symp. 135, Interstellar Dust, ed. L. J. Allamandola & A. G. G. M. Tielens (Dordrecht: Kluwer), 239
Vrba, F. J., Coyne, G. V., & Tapia, S. 1993, AJ, 105, 1010
Whittet, D. C. B., Gerakines, P. A., Hough, J. H., & Shenoy, S. S. 2001, ApJ, 547, 872
Whittet, D. C. B., & van Breda, I. G. 1978, A&A, 66, 57
Williams, J. P., Blitz, L., & McKee, C. F. 2000, in Protostars and Planets IV, ed. V. Mannings, A. P. Boss, & S. S. Russel (Tucson: Univ. Arizona Press), 97
Yun, J. L., & Clemens, D. P. 1995, AJ, 109, 742